Path Integral Monte Carlo and Density Functional Molecular Dynamics Simulations of Warm, Dense $MgSiO_3$

Felipe González-Cataldo,[1,*] François Soubiran,[2,1] Henry Peterson,[1] and Burkhard Militzer[1,3]

[1]*Department of Earth and Planetary Science, University of California, Berkeley, California 94720, USA*
[2]*Laboratoire de géologie de Lyon, CNRS UMR 5276, Ecole Normale Supérieure de Lyon, Université Claude Bernard Lyon 1, 46 Allée d'Italie, 69364 Lyon Cedex 07, France*
[3]*Department of Astronomy, University of California, Berkeley, California, USA*

(Dated: December 3, 2019)

In order to provide a comprehensive theoretical description of $MgSiO_3$ at extreme conditions, we combine results from path integral Monte Carlo (PIMC) and density functional molecular dynamics simulations (DFT-MD) and generate a consistent equation of state for this material. We consider a wide range of temperature and density conditions from 10^4 to 10^8 K and from 0.321 to 64.2 g cm^{-3} (0.1- to 20-fold the ambient density). We study how the L and K shell electrons are ionized with increasing temperature and pressure. We derive the shock Hugoniot curve and compare with experimental results. Our Hugoniot curve is in good agreement with the experiments, and we predict a broad compression maximum that is dominated by the K shell ionization of all three nuclei while the peak compression ratio of 4.70 is obtained when the Si and Mg nuclei are ionized. Finally we analyze the heat capacity and structural properties of the liquid.

I. INTRODUCTION

The equation of state (EOS) of materials in the regime of warm dense matter is fundamental to model planetary interiors [1–3], astrophysical processes [4, 5], interpret shock-wave experiments [6, 7], and understand the physics of inertial confinement fusion experiments [8–11]. Novel experiments and computational techniques have allowed the study of the properties of matter at extreme conditions and produce EOS of materials in a wide range of temperatures and densities. Among the computational techniques are path integral Monte Carlo (PIMC) simulations [12–16], which have provided a unique insight into the properties of matter at extreme temperature and pressure conditions relevant to fusion experiments, where a detailed description of dense plasmas is required to understand the underlying physics. There has been a considerable effort to study the properties of materials heavier than hydrogen and helium in the warm dense matter regime with these techniques, materials such as lithium fluoride [17], boron [8], aluminum [18], hydrocarbons [19], and superionic water [20, 21]. However, the properties of triatomic materials, such as $MgSiO_3$, have not been studied.

Enstatite ($MgSiO_3$) is key material for planetary science and shock physics [7, 22–25]. It is one of the few silicate minerals that has been observed in crystalline form outside the Solar System [26], and is assumed to be one fundamental building block in planetary formation [27, 28]. Along with forsterite (Mg_2SiO_4), it is one of the most abundant materials in the Earth's mantle, and it is also expected to be present in super-Earth planets [26, 29]. The properties of silicates at conditions existing at planetary interiors are poorly known because reaching Mbar pressures and 5000–10000 K temperatures in the laboratory presents a serious challenge.

Recent ramp compression experiments at the National Ignition Facility (NIF) and the *Ligne d'Intégration Laser* (LIL) facility have explored the properties of silicates and iron at the conditions encountered in planetary interiors, studying their metallization and dissociation up to 15 Mbar [3, 30, 31]. Under ramp compression, the system follows a thermodynamic path that is quasi-isentropic [30, 32–35], as the heat generated is significantly lower than in shock compression. This is ideal to reach the pressures and temperatures present at the interior of super-Earth planets [2, 36]. How close the compression path follows an isentrope depends on the sample properties and on the details of the experiments. It is therefore beneficial to compute the isentropes with first-principle computer simulations in order to guide interpretations of the experimental findings. Isentropes are also of fundamental importance in planetary science because planets cool convectively, thus, most of the interiors are assumed to be adiabatic [2, 29, 36, 37]. However, there are known exceptions, such as the boundary layer in the Earth mantle, where temperature rises superadiabatically because of the high mantle viscosity, and the outermost atmospheres of giant planets, where heat is carried radiatively.

In recent laser-shock experiments, the equations of state of enstatite and forsterite on the principal Hugoniot curve have been measured up to 950 GPa and 30000 K [28, 38, 39], suggesting a metallic-like behavior in liquid $MgSiO_3$ over a large pressure-temperature regime. Finding signatures of melting along the Hugoniot curves of silicates is fundamental to understand the dynamics of the Earth's lower mantle [31, 40], as well as understanding the rich phase diagram of $MgSiO_3$, which undergoes a series of phase transitions before partitioning into Mg and SiO_2 [41, 42]. However, the behavior of this mineral at temperatures relevant to the conditions of shock experiments where ionization of the electronic shells take place, is unknown.

Recent *ab initio* simulations have shown that liquid silicates can exhibit very high conductivity at high pressure, which implies that super-Earths can generate magnetic fields in their mantle [43]. Therefore, it is desirable to have a first-principles EOS derived for much higher temperature and density conditions that span regimes of condensed matter, warm dense matter (WDM), and plasma physics in order to be used as a reference for shock experiments and hydrodynamic simulations. In recent works, a first-principles framework has been developed to compute consistent EOS across a wide range of density-temperature regimes relevant to WDM by combining results from state-of-the-art path integral Monte Carlo (PIMC) and DFT-MD simulation methods for first- [44] and second-row [45, 46] elements.

* f_gonzalez@berkeley.edu

In this paper, we apply our PIMC and DFT-MD methods to compute the EOS and plasma properties of $MgSiO_3$ across a wide density-temperature range. We study the evolution of the plasma structure and ionization over the WDM regime. Finally, we compare our PIMC/DFT-MD shock Hugoniot curves with widely used models and experiments.

II. METHODS

We perform first-principles computer simulations of warm-dense $MgSiO_3$ using two different simulation methods: path integral Monte Carlo (PIMC) and Kohn-Sham density functional theory molecular dynamics (DFT-MD) simulations. PIMC is a state-of-the-art first-principles technique for computing the properties of interacting quantum systems at finite temperature. The basic techniques for simulating bosonic systems were developed in Ref. [47] and reviewed in Ref. [48]. Subsequently the algorithm was generalized to fermion systems using the *restricted* path integral method. The first results of this simulation method were reported in the seminal work on liquid ^{3}He [49] and dense hydrogen [14]. A review of the algorithm is given in Ref. [50]. In subsequent articles, this method was applied to study hydrogen [16, 51–54], helium [55–57], hydrogen-helium mixtures [58] and one-component plasmas [59–61]. In recent years, the method was extended to simulate plasmas of various first-row elements [8, 17, 62–65] and with the development of Hartree-Fock nodes, the simulations of second-row elements became possible [18, 45, 66, 67].

This method is based on the thermal density matrix of a quantum system, $\hat{\rho} = e^{-\beta\hat{\mathcal{H}}}$, that is expressed as a product of higher-temperature matrices by means of the identity $e^{-\beta\hat{\mathcal{H}}} = (e^{-\tau\hat{\mathcal{H}}})^M$, where $\tau \equiv \beta/M$ represents the time step of a path integral in imaginary time. The path integral emerges when the operator $\hat{\rho}$ is evaluated in real space,

$$\langle \mathbf{R}|\hat{\rho}|\mathbf{R}'\rangle = \frac{1}{N!}\sum_{\mathcal{P}}(-1)^{\mathcal{P}} \oint_{\mathbf{R}\to\mathcal{P}\mathbf{R}'} \mathbf{dR}_t\, e^{-S[\mathbf{R}_t]}. \qquad (1)$$

Here, we have already summed over all permutations, $\mathcal{P}$, of all N identical fermions in order project out all antisymmetric states. For sufficiently small time steps, τ, all many-body correlation effects vanish and the action, $S[\mathbf{R}_t]$, can be computed by solving a series of two-particle problems [47, 68, 69]. The advantage of this path integral approach is that all many-body quantum correlations are recovered through the integration over all paths. The integration also enables one to compute quantum mechanical expectation values of themodynamic observables, such as the kinetic and potential energies, pressure, pair correlation functions and the momentum distribution [48, 70]. Most practical implementations of the path integral techniques rely on Monte Carlo sampling techniques due to the high dimensionality of the integral and, in addition, one needs to sum over all permutations. The method becomes increasingly efficient at high temperature because the path the length of the paths scales like $1/T$. In the limit of low temperature, where few electronic excitations are present, the PIMC method becomes computationally demanding and the MC sampling can become inefficient. However, the PIMC method avoids any exchange-correlation approximation and the calculation of single-particle eigenstates, which are deeply embedded in all Kohn-Sham DFT calculations.

The only uncontrolled approximation within fermionic PIMC calculations is the use of the fixed-node approximation, which restricts the paths in order to avoid the well-known fermion sign problem [13, 49, 50]. Addressing this problem in PIMC is crucial, as it causes large fluctuations in computed averages due to the cancellation of positive and negative permutations in Eq. (1). We solve the sign problem approximately by restricting the paths to stay within our Hartree-Fock nodes [18, 45, 64]. We enforced the nodal constraint in small imaginary time steps of $\tau = 1/8192$ Ha, while the pair density matrices were evaluated in steps of 1/1024 Ha. This results in using between 1200 and 12 time slices for the temperature range that studied with PIMC simulations here. These choices converged the internal energy per atom to better than 1%. We have shown the associated error is small for relevant systems at sufficiently high temperatures [13, 44, 50].

On the other hand, Kohn-Sham DFT-MD [71–73] is a well-established theory that has been widely applied to compute the EOS of condensed matter as well as warm and hot, dense plasmas [8, 74–76]. It is a suitable option to derive the EOS because it accounts for both the electronic shells and bonding effects. The main approximation in DFT-MD is the use of an approximate exchange-correlation (XC) functional. Although at temperatures relevant to WDM, the error in the XC functional is small relative to the total energy, which is the most relevant quantity for the EOS and derivation of the shock Hugoniot curve [77].

Still, standard Kohn-Sham DFT-MD simulations become computationally inefficient at high temperatures ($T > 10^6$ K) because it requires one to explicitly compute all fully and partially occupied electronic orbitals, which becomes increasingly demanding as temperature increases. The number of occupied bands increases unfavorably with temperature, scaling approximately as $\sim T^{3/2}$. Accuracy is also compromised at high temperatures. The excitation of the inner electrons, which are typically frozen by the pseudopotentials, may contribute to the pressure and energy of the system as inner electronic shells become partially ionized with increasing temperature. In contrast, PIMC is an all-electrons method that increases in efficiency with temperature (scaling as $1/T$) as quantum paths become shorter and more classical in nature.

Consequently, our approach consist in performing simulations along different isochores of $MgSiO_3$, using PIMC at high temperatures (1.3×10^6 K $\leq T \leq 5.2 \times 10^8$ K) and DFT-MD at low temperatures (1.0×10^4 K $\leq T \leq 1.0 \times 10^6$ K). We show the two methods produce consistent results at overlapping temperature regimes.

For PIMC simulations, we use the CUPID code [78] with Hartree-Fock nodes. For DFT-MD simulations, we employ Kohn-Sham DFT simulation techniques as implemented in the Vienna Ab initio Simulation Package (VASP) [79] using the projector augmented-wave (PAW) method [80, 81], and molecular dynamics is performed in the NVT ensemble, regulated with a Nosé thermostat. Exchange-correlation effects are described using the Perdew, Burke, and Ernzerhof [82] (PBE) generalized gradient approximation (GGA). The pseudopotentials used in our DFT-MD calculations freeze the electrons of the 1s orbital, which leaves 10, 12, and 6 valence electrons for Mg, Si, and O atoms, respectively. Electronic wave functions are expanded in a plane-wave basis with a energy cut-off as high as 7000 eV in order to converge total energy. Size convergence tests with up to a 65-atom simulation cell at temperatures of 10 000 K and above indicate that pressures are converged

to better than 0.6%, while internal energies are converged to better than 0.1%. We find, at temperatures above 500 000 K, that 15-atom supercells are sufficient to obtain converged results for both energy and pressure, since the kinetic energy far outweighs the interaction energy at such high temperatures [18, 83]. The number of bands in each calculation was selected such that orbitals with occupation as low as 10^{-4} were included, which requires up to 14 000 bands in an 15-atom cell at 2×10^6 K and two-fold compression. All simulations are performed at the Γ point of the Brillouin zone, which is sufficient for high temperature fluids, converging total energy to better than 0.01% compared to a grid of k-points.

III. EQUATION OF STATE RESULTS

In this section, we combine results from our PIMC and DFT-MD simulations in order to provide a consistent EOS table spanning the warm dense matter and plasma regimes. Computations were performed for a series of densities and temperatures ranging from 0.321–64.16 g cm^{-3} and 10^4–10^8 K. The full range of our EOS data points is shown in temperature-density space in Fig. 1 and in temperature-pressure space in Fig. 2.

In order to put the VASP PBE pseudopotential energies on the same scale as the all-electron PIMC calculations, we shifted all VASP DFT-MD energies by $\Delta E = -713.777558$ Ha/atom. This shift was derived by performing all-electron calculations for the isolated non-spin-polarized Mg, Si, and O atoms with the OPIUM code [84] and comparing the results with corresponding VASP calculations.

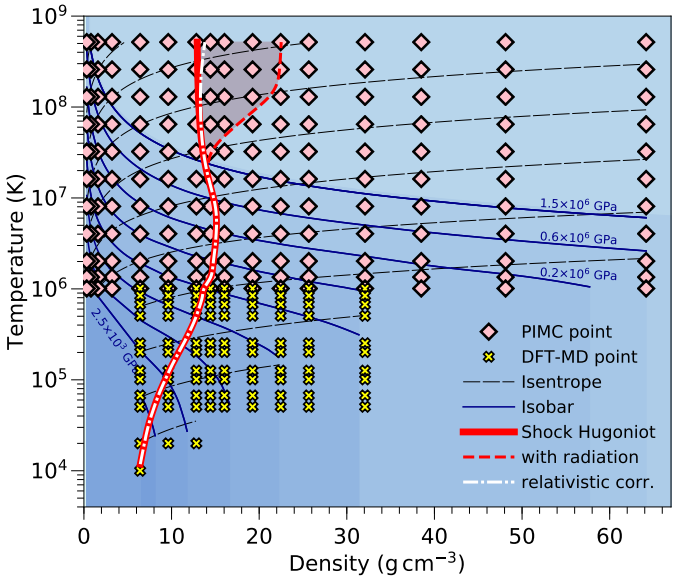

FIG. 1. Temperature-density conditions of our DFT-MD and PIMC simulations along with computed isobars, isentropes and three principal shock Hugoniot curve that were derived for an initial density of $\rho_0 = 3.207911$ g cm^{-3} ($V_0 = 51.965073$ Å/f.u.).

In order to analyze the consistency of our EOS data sets, Figs. 3 and 4 display the pressure and internal energy, respectively, along three isochores from PIMC, DFT-MD, and the classical Debye-Hückel plasma model [88] as a function of temperature. The pressures, P, and internal energies, E, are plotted relative to a fully ionized Fermi gas of electrons and ions with pressure P_0 and internal energy E_0 in order to compare only the excess contributions that are the result from the particle interactions.

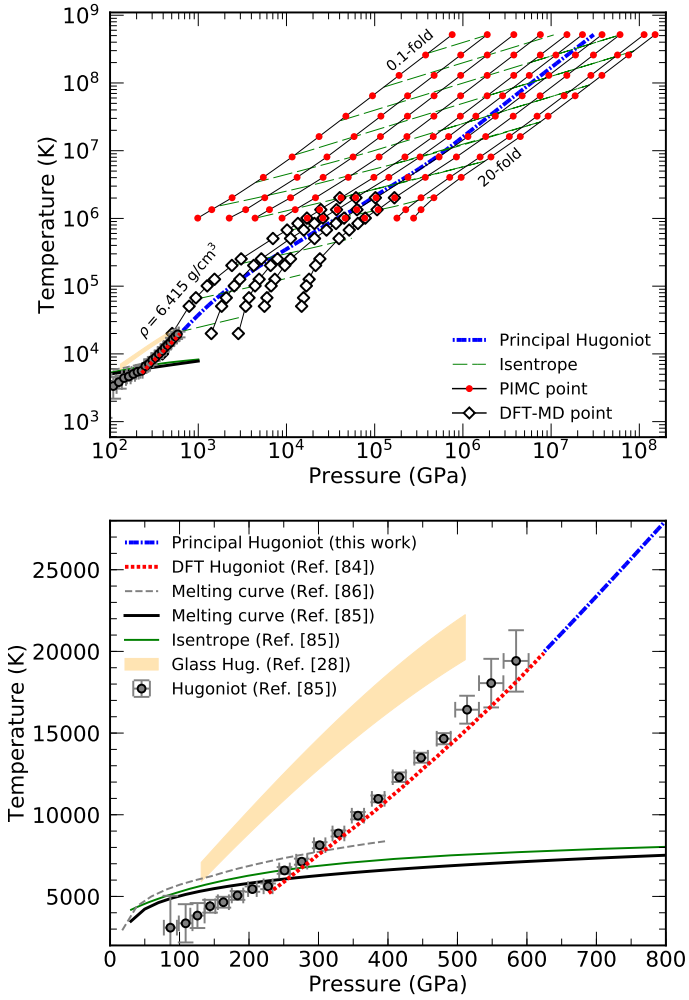

FIG. 2. Temperature-pressure conditions for the PIMC and DFT-MD calculations along isochores corresponding to the densities of 0.1-fold (0.321 g cm^{-3}) to 20-fold (64.20 g cm^{-3}). The blue dash-dotted line shows the principal Hugoniot curve of $MgSiO_3$ obtained from our simulations, using an initial density of $\rho_0 = 3.207911$ g cm^{-3} ($V_0 = 51.965073$ Å/f.u.). The red dashed line corresponds to the Hugoniot curve from Ref. [85], calculated from DFT-MD simulations. Experimental measurement of the principal Hugoniot curve from Ref. [86], an isentrope derived from this experiment (solid green line), and the Hugoniot curve for $MgSiO_3$ glass [28] (orange region) are shown for reference. The melting line of $MgSiO_3$ derived from two-phase simulations [87] is shown in dashed grey line, while the melting curve derived from shock experiments [86] is represented by the thick black line.

With increasing temperature, these contributions gradually decrease from the strongly interacting condensed matter regime, where chemical bonds and bound states dominate, to the weakly interacting, fully ionized plasma regime. There, the PIMC results converge to predictions from the classical Debye-Hückel model. As expected, the Debye-Hückel model becomes inadequate for lower temperatures ($T < 10^7$ K) since it fails to treat bound electronic

states. While the temperature range over which PIMC EOS data are needed to fill the gap between DFT-MD and Debye-Hückel model (approximately from 2×10^6 to 1×10^7 K) is relatively small compared to the entire temperature range under consideration, this temperature interval encompasses significant portions of K shell ionization regime, which is precisely where the full rigor of PIMC simulations are needed to acquire an accurate EOS table.

Figs. 3 and 4 show a consistent EOS over a wide density-temperature range, where PIMC and DFT-MD simulations provide consistent results in the overlapping range of 1–2 $\times 10^6$ K. At these

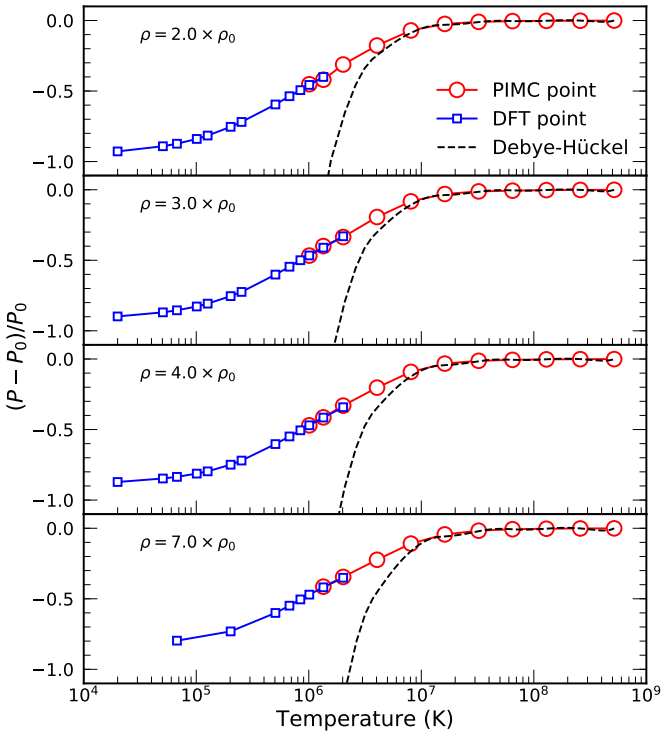

FIG. 3. Excess pressure as a function of temperature relative to the ideal Fermi gas, computed with PIMC, DFT-MD, and the Debye-Hückel plasma model. The results are plotted for densities of (a) 6.4, (b) 3.651, (c) 7.582, and (d) 15.701 g cm^{-3}.

temperatures, the pressures predicted by PIMC and DFT-MD differ by less than 3%, with the exception of 10^6 K at 7-fold compression, where we obtained a difference of 5.3% in the pressure. We attribute this difference to the known loss of accuracy of PIMC at low temperature. However, we do not observe this large difference at any other density.

The total energies predicted by DFT-MD are also in good agreement with those predicted by PIMC (see Fig. 4), with differences generally between 1.5–6.5 Ha/atom (3–6%). Larger energy differences are observed at 2×10^6 K, where DFT-MD seems unable to reproduce the energies predicted by PIMC, within the error bars. At this temperature, we observe a systematic energy offset of 6.5–8.5 Ha/atom (11–23%) as the density increases. These errors are mostly due to the use of pseudopotentials used in DFT simulations, where inner electrons are bound to the nucleus and cannot be excited to contribute to the energy, resulting in an underestimation of the total

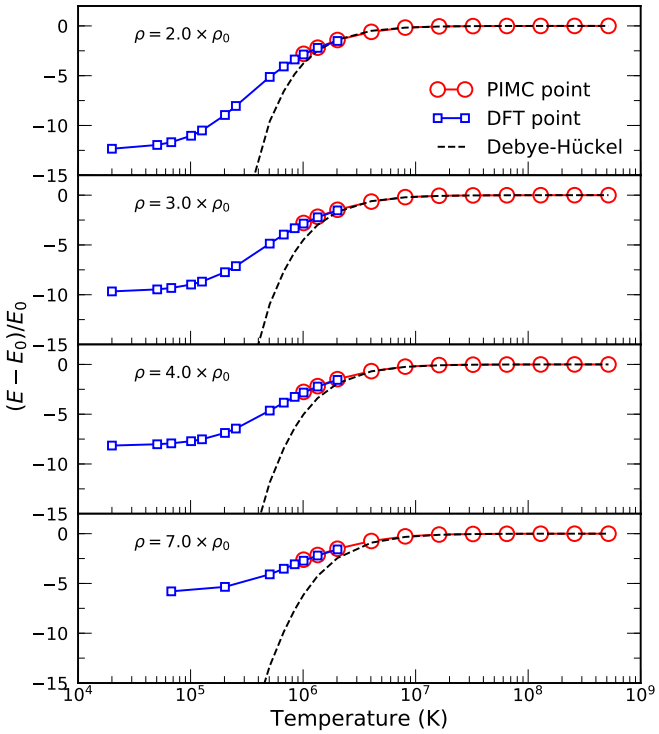

FIG. 4. Excess internal energy, relative to the ideal Fermi gas, computed with PIMC, DFT-MD, and the Debye-Hückel plasma model. As in the corresponding Fig. 3, the results are plotted for densities of (a) 6.4, (b) 3.651, (c) 7.582, and (d) 15.701 g cm^{-3} as a function of temperature.

energy of the system. We will come back to this point when we discuss the ionization of the electronic shells (Fig. 8) in the next section.

In Fig. 5 and 6, we show the total energy and pressure as a function of density for a number of temperatures. While pressure increases with density, we find that all the $E(\rho)_T$ curves have a minimum. With increasing temperature, the location of this minimum shifts towards high densities. At low density, the slope $\left(\frac{\partial E}{\partial \rho}\right)_T$ is negative because the system is more ionized, as we will discuss in section IV. At high density, the slope $\left(\frac{\partial E}{\partial \rho}\right)_T$ is positive for two possible reasons. First there is the confinement effect, which increases the kinetic energy of the free electrons and, second, the orbitals of the bound electrons hybridize and may even be pushed into the continuum of free electronic states, which is commonly referred to as pressure ionization.

Using Maxwell relations, one can infer that this energy minimum corresponds to the point where the thermal pressure coefficient, $\beta_V \equiv \frac{\partial P}{\partial T}|_V$, is equal to the ratio between pressure and temperature, because

$$\left(\frac{\partial E}{\partial V}\right)_T = T\left[\left(\frac{\partial P}{\partial T}\right)_V - \frac{P}{T}\right] = T\left[\beta_V - \frac{P}{T}\right] = 0. \quad (2)$$

This derivative vanishes if

$$\left(\frac{\partial \ln P}{\partial \ln T}\right)_V = 1\,. \quad (3)$$

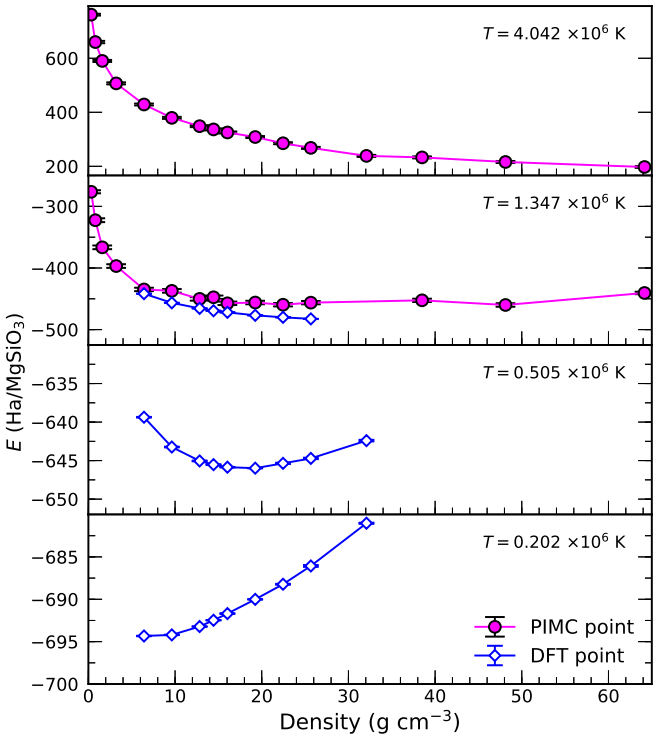

FIG. 5. Total internal energy as a function of density, computed with PIMC and DFT-MD.

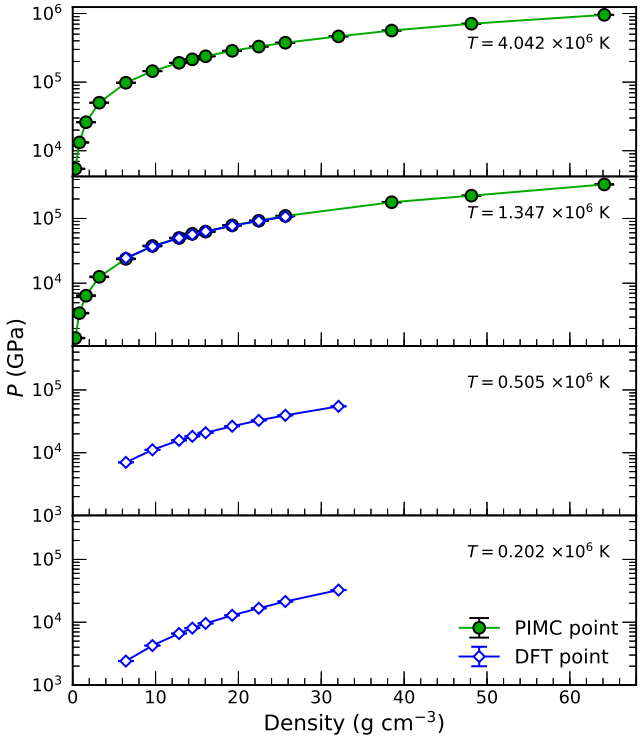

FIG. 6. Pressure as a function of density, computed with PIMC and DFT-MD.

This condition is trivially fulfilled for an ideal gas, that satisfies $\frac{\partial E}{\partial V}\big|_T = 0$ everywhere. At very high temperature, where ionization is complete, we find that $MgSiO_3$ starts behaving similar to an ideal gas and the isochores, that we show in $\ln T$-$\ln P$ space in Fig. 2, have a slope of approximately 1. When Eq. 3 is satified, we obtain a minimum in the $E(\rho)_T$ curve. For example, at $T = 0.202 \times 10^6$, we find an energy minimum in Fig. 5 around $\rho \approx 6.42$ g cm^{-3} while $\frac{\partial \ln P}{\partial \ln T}\big|_V$ becomes 1 in Fig. 2 for the same conditions.

We note that the overall agreement between PIMC and DFT-MD provides validation for the use of zero-temperature exchange correlation functionals in warm dense matter applications and the use of the fixed-node approximation in PIMC in the relevant temperature range. At temperatures lower than the overlapping regime, PIMC results become inconsistent with DFT-MD results because the nodal approximation in PIMC simulations is no longer appropriate. Nevertheless, the validity of our EOS is not affected by these discrepancies, as we are able to build a consistent interpolation that spans across all temperatures.

The isochoric Grüneisen parameter,

$$\gamma = V\left(\frac{\partial P}{\partial E}\right)_V = \frac{V}{C_V}\left(\frac{\partial P}{\partial T}\right)_V = -\left(\frac{\partial \ln T}{\partial \ln V}\right)_S, \qquad (4)$$

is a useful quantity to model material properties, since it usually does not significantly depend on temperature. It is the key parameter of the Mie-Grüneisen model, which is often used in shock experiments to model the EOS of solids and liquids [38, 40, 86, 89] and obtain related properties, such as the specific heat, melting temperature and, in general, to infer how pressure depends on temperature along different thermodynamic paths. The Grüneisen parameter can also be inferred from the shock Hugoniot curve [86] and, by means of Eq. (4), can be used to obtain isentropic paths, such as the temperature profile in magma oceans and ramp compression curves [30, 33].

In Fig. 7 we show the Grüneisen parameter, calculated from our EOS using Eq. (4), as a function of volume at different temperatures. First principles simulations and experiments report that in liquid $MgSiO_3$, contrary to the usual trend in solids, γ increases upon compression [40, 90] for temperatures up to 8000 K and volumes from 25.8–64.6 Å^3/f.u. We also observe this behavior in most of the temperatures analyzed in our study, as shown in Fig. 7, with the exception of 2×10^4 K, where we observe that γ decreases with upon compression. However, this behavior changes dramatically at higher temperatures. At 5×10^4 K, γ is almost independent of volume, and above 7×10^4 K, it increases upon compression, as it was observed in experiments at much lower densities and temperatures. Our results indicate that the Grüneisen parameter can decrease along an isentrope for temperatures below 3×10^4 K, but increases along the isentropes with temperatures between 4×10^4 and 4×10^5 K.

At even higher temperatures the dependence on volume becomes weaker, and at 16×10^6 K, γ decreases upon compression. If the temperature is high enough to ionize the K shell of the atoms, as we will disccuss in the next section, the plasma behaves similar to a gas of free particles, described by the equation of state $E = \frac{3}{2}PV$ and the Grüneisen parameter $\gamma_0 = 2/3$, which is independent of both temperature and density.

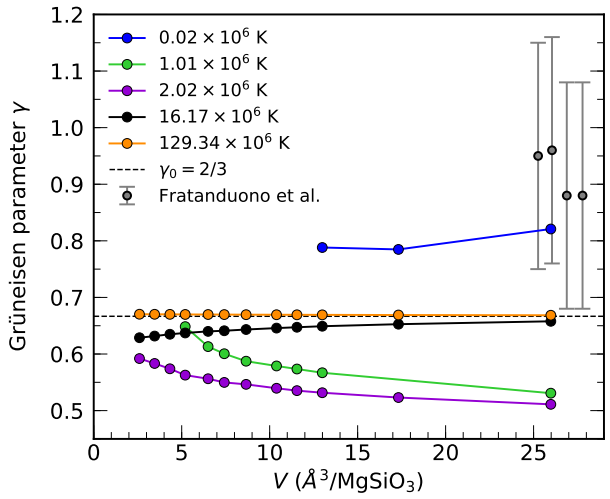

FIG. 7. Grüneisen parameter of $MgSiO_3$ as a function of volume for different temperatures. The horizontal, dashed line represents high temperature limit (the Grüneisen parameter of the ideal gas), $\gamma_0 = 2/3$. Values of Grüneisen parameter along the principal Hugoniot from shock compression experiments [86] (shown in grey circles with error bars) correspond to pressures between 230–380 GPa and temperatures between 6200–10000 K.

IV. K SHELL IONIZATION

From PIMC simulations, a measure of the degree of ionization can be obtained from the integrated nucleus-electron pair correlation function, $N(r)$, given by

$$N(r) = \left\langle \frac{1}{N_I} \sum_{e,I} \Theta(r - \|\vec{r}_e - \vec{r}_I\|) \right\rangle , \qquad (5)$$

where $N(r)$ represents the average number of electrons within a sphere of radius r around a given nucleus of atom of type I. The summation includes all electron-nucleus pairs and Θ represents the Heaviside function. Fig. 8 shows the integrated nucleus-electron pair correlation function for temperatures from 1×10^6 K to 65×10^6 K and densities from 0.321 g cm^{-3} (0.1-fold) to 64.20 g cm^{-3} (20-fold compression). For comparison, the $N(r)$ functions of an isolated nucleus with a doubly occupied 1s orbital were included. Unless the 1s state is ionized, its contribution will dominate the $N(r)$ function at small radii of $r < 0.2$ Bohr radii. For larger radii, contributions from other electronic shells and neighboring nuclei will enter. Still, this is the most direct approach available to compare the degree of 1s ionization of the three nuclei.

At 0.1-fold compression, the comparison with the corresponding curves for the isolated nuclei shows that the ionization of the 1s states of the Si and Mg nuclei occurs over the temperature interval from 2.0 to 4.0×10^6 K. Conversely, the ionization of 1s state of the oxygen nuclei starts already at 1.0×10^6 K, which reflects the difference in binding energy that scales with the square of the nuclear charge, Z. Consistent with this interpretation, one finds that for 4.0 $\times10^6$ K the Mg nuclei are slightly more ionized than the heavier Si nuclei, while the ionization of the oxygen nuclei is essentially complete at this temperature.

When the density is increased from 0.1- to 1.0-fold compression (second row of panels in Fig. 8), the degree of 1s ionization is reduced. For all three nuclei, the $N(r)$ functions at small r are closer to doubly occupied 1s state than they were before. This trend continues as we increase the density to 4.0 and 20-fold compression. The degree of 1s ionization is consistently reduced with increasing density when the results are compared for the same temperature. Most notably we find the silicon 1s state to be almost completely ionized at 0.1-fold compression and 8.1 $\times10^6$ K while very little ionization is observed at this temperature for 20-fold compression. Similarly, we find almost no ionization of the oxygen 1s state at 20-fold compression and 2.0×10^6 K, while this state is significanly ionized for 0.1-fold compression at the same temperature.

For temperatures higher than 32×10^6 K, thermal excitations are enough to fully ionize all atomic species at any of the densities explored, and the electrons become unbound free particles. This picture is consistent with our Grüneisen parameter calculations, which show (see Fig. 7) that the system has already reached the limiting value of $\gamma_0 = 2/3$ at this temperature, consistent with the ideal gas. We consistently find the degree of 1s ionization to decrease as we lower the temperature or increase the density in our PIMC simulations. The trend with density can be interpreted as an entropy-driven 1s ionization, that can be described by Saha ionization equilibrium [91]. With decreasing density, more free-particle states become available and thus ionization equilibrium shifts towards higher ionization.

One would expect to find the opposite trend at very high density, where Pauli exclusion effects cause the 1s state energy to rise, generating a higher degree of 1s ionization. However, in our simulations the density is not sufficiently high for the 1s states of the different nuclei to significantly overlap and cause ionization by this mechanism. These results are compatible with the ionization profile of pure oxygen [92], where no pressure ionization of the K shell at 1×10^6 K was observed in a similar range of densities. This analysis does not rule out the possibility of pressure ionization to occur for higher-energy, more delocalized electronic states.

We find no significant ionization of the 1s orbital at $T = 10^6$ K at any of the densities explored, which indicates that these inner electrons do not contribute to the thermodynamic properties of the system at this temperature. DFT pseudopotentials with a helium core should, therefore, be sufficient to represent $MgSiO_3$ at these conditions accurately. This is not the case for lighter materials, such as B and LiF [8, 17], where a temperature 10^6 K is enough to cause partial ionization of the K shell due to the smaller number of electrons that those ions have. Heavier elements such as aluminium, to the contrary, require temperatures above 4×10^6 K to ionize the 1s electrons.

V. PAIR CORRELATION FUNCTIONS

The radial pair correlation function $g_{\alpha\beta}(r)$ is a measure of the atomic coordination, which depends on temperature and density. It can be interpreted as the probability of finding an particle of type α at distance r from a particle of type β. The nuclear pair-correlation function is given by

$$g_{\alpha\beta}(r) = \frac{V}{4\pi r^2 N_\alpha N_\beta} \left\langle \sum_{i=1}^{N_\alpha} \sum_{j\neq i}^{N_\beta} \delta\left(r - \|\vec{r}_{ij}\|\right) \right\rangle , \qquad (6)$$

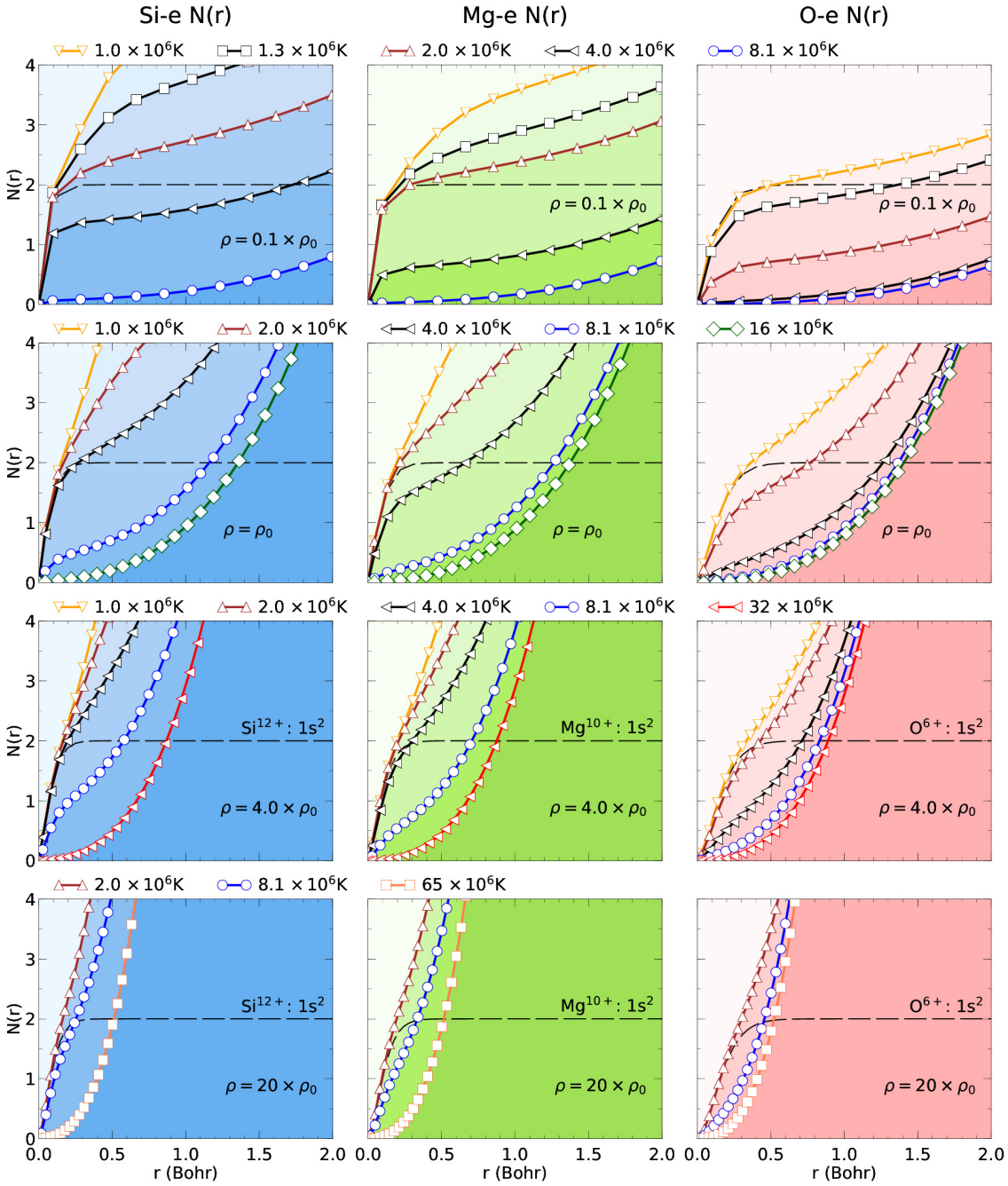

FIG. 8. Integrated nuclear-electron pair correlation, functions $N(r)$, computed with PIMC simulations. The three columns correspond to the Mg, Si and O nuclei while the four rows show results for the densities of 0.321 (0.1-fold compression), 3.21 (1.0-fold compression), 12.83 (4.0-fold compression), and 64.16 g cm^{-3} (20-fold compression). For given density, results are shown for the same set of temperatures for all three nuclei. However, these temperatures adjusted with increasing density because the degree of ionization is density dependent. The $N(r)$ represent the average of number of electrons contained within a sphere of radius, r, around a given nucleus. For comparison we show the corresponding functions with thin dashed lines for isolated nuclei with double occupied 1s core states that we computed with the GAMESS software [93].

where N_α and N_β are the total number of nuclei of type α and β, respectively, V is the cell volume, and $\vec{r}_{ij} = \vec{r}_i - \vec{r}_j$ the separation between atoms i and j.

In Fig. 9, we compare the $N(r)$ and $g(r)$ functions that we derived with DFT-MD simulations for one T-ρ point. The purpose of this comparison is to analyze how many nearest neighbors contribute to the various shells of neighboring atoms that appear as maxima in the pair correlation functions. The $N(r)$ function can be derived by applying Eq. 5 to different pairs of nuclei. When r is set to the first $g(r)$ minimum, the value of $N(r)$ is commonly referred to as coordination number. The six $N(r)$ functions in Fig. 9 are split into two groups. Functions that involve oxygen nuclei are much higher because there are three times as many nuclei that contribute. The Si-O $N(r)$ function rises most quickly with increasing

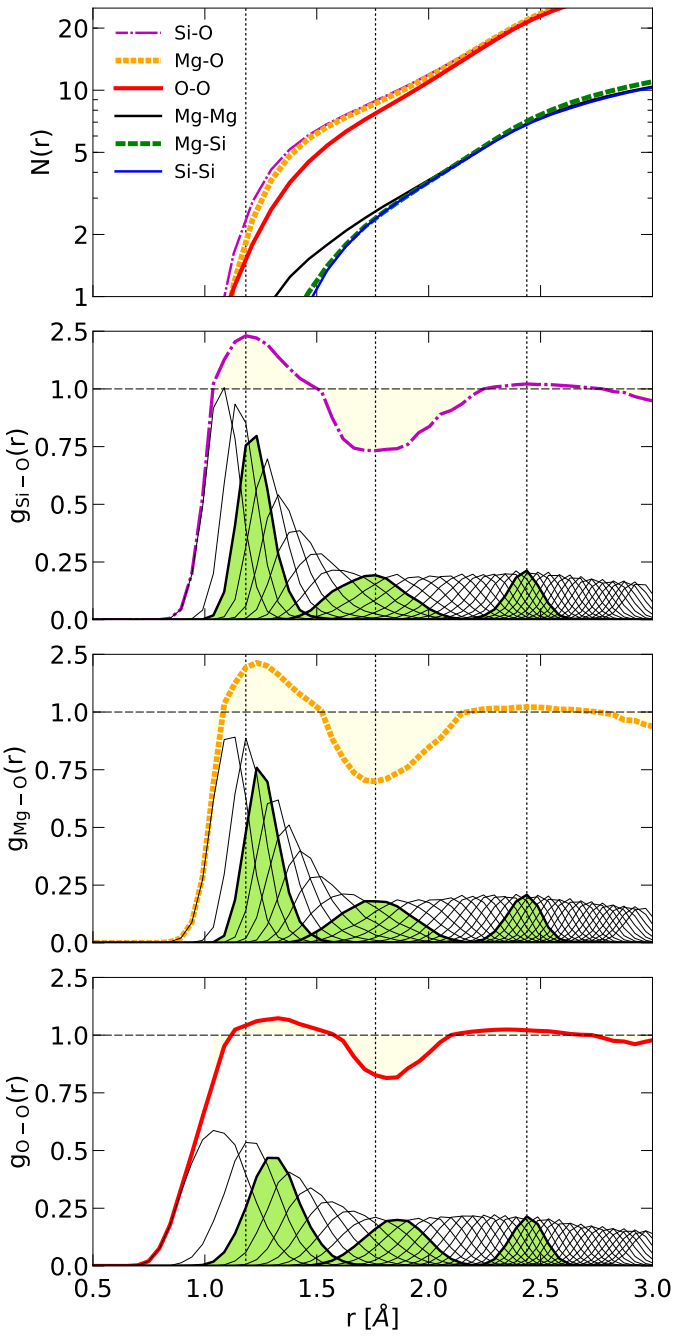

FIG. 9. $N(r)$ and $g(r)$ correlation functions for liquid $MgSiO_3$ at T = 50 523 K and ρ=19.247 g cm^{-3} (6-fold compression). In the three lower panels, the $g(r)$ functions were split into the contributions from the nth nearest neighbors. The functions of the 3rd, 9th and 21st neighbors were shaded because their locations respectively correspond to first maximum, first minimum, and second maximum of the Si-O $g(r)$ function. Their locations are also marked by the vertical dotted lines. To improve the readability, the scales of the Y axes in the three lower panels were split into two separate linear parts, one from 0 and 1, and a compressed region from 1 and 2.5.

r, reaching a value of N=2.44 neighbors for $r = 1.18$ Å, where the corresponding $g(r)$ function reaches its first maximum of 2.38. This is the most positive nuclear correlation in this dense, hot fluid. It still carries a signature of the strong Si-O attraction that leads to the formation of rigid SiO_4 tetrahedra that dominate the coordination in $MgSiO_3$ liquids and solids at much lower temperature and pressure [94]. Nevertheless $MgSiO_3$ liquid is much more disordered at the extreme conditions that we consider in this article. If one splits the $g(r)$ function into the contributions from the nth nearest neighbor, one finds that the first maximum of total $g(r)$ functions at $r = 1.18$ Å falls in between the peaks of the contributions from the second and third neighbors, as one would have expected for a value of N=2.44. Less expected was how much overlap there is between contributions from various neigbors. At $r = 1.18$ Å there are contributions from up to five oxygen atoms. Similar if one goes out to the first $g(r)$ minimum at $r = 1.76$ Å, one finds that contributions from the 9th neighbor dominate but contributions from the 6th through 12th are still relevant. At the second $g(r)$ maxium, located at $r = 2.44$ Å, contributions from the 21st neighbor dominate.

As expected, we also find a positive correlation between Mg and O nuclei but it is not quite as strong as that between Si and O nuclei. The first $g_{\mathrm{Mg-O}}(r) = 2.28$ maximum occurs at slightly larger distance of $r = 1.23$ Å. It falls again in between peaks of the contributions from the second and third neighbors.

The oxygen-oxygen pair correlation function is a bit different but still positive. Its first maximum is much lower, $g_{\mathrm{O-O}}(r) = 1.44$, and occurs only at large separations of $r = 1.33$ Å. It coincides with the peak in the $g(r)$ contribution function from the third neighbor.

In figure 10, we compare the nuclear pair correlation function for 2-, 5-, 6- and 10-fold compression and two temperatures of 50×10^3 and $T = 202 \times 10^3$ K. At 2-fold compression, the $g(r)$ function shows the profile of a typical liquid. The Mg-O and Si-O bond lengths are approximately equal as the location of respective first peaks indicate. As density increases, the atoms get closer together and these two peaks shift, leading to a stronger shortening for the Si-O bond than for Mg-O bond. For the other pairs of species, the first peak of the radial distribution function localizes at smaller distances, becoming more pronounced as the density increases. This is evidence for stronger correlations at high density. This trend is also seen for the Mg-Mg, Si-Si, and O-O pair correlation functions.

When the temperature is increased from 50×10^3 K to 202×10^3 K, the correlation effects are reduced. Most notably one finds that the Mg-Si, Mg-O, and Si-O pair correlation functions become fairly similar to each other, while they were rather different at 50×10^3 K.

VI. SHOCK HUGONIOT CURVES

Dynamic shock compression experiments are a direct way to determine the equation of state of hot, dense fluids by only measuring the shock and particle velocities. Such experiments are often used to determine the principal Hugoniot curve, which is the locus of all final states that can be obtained from different shock velocities [86].

Initially, the sample material has the internal energy, pressure, and volume, $\{E_0, P_0, V_0\}$. Under shock compression, the material changes to a final state denoted by $\{E(\rho,T), P(\rho,T), V\}$. The conservation of mass, momentum, and energy across the shock front leads to the Rankine-Hugoniot relation [95],

$$[E(\rho,T) - E_0] + \frac{1}{2}\,[P(\rho,T) + P_0]\,[V - V_0] = 0. \qquad (7)$$

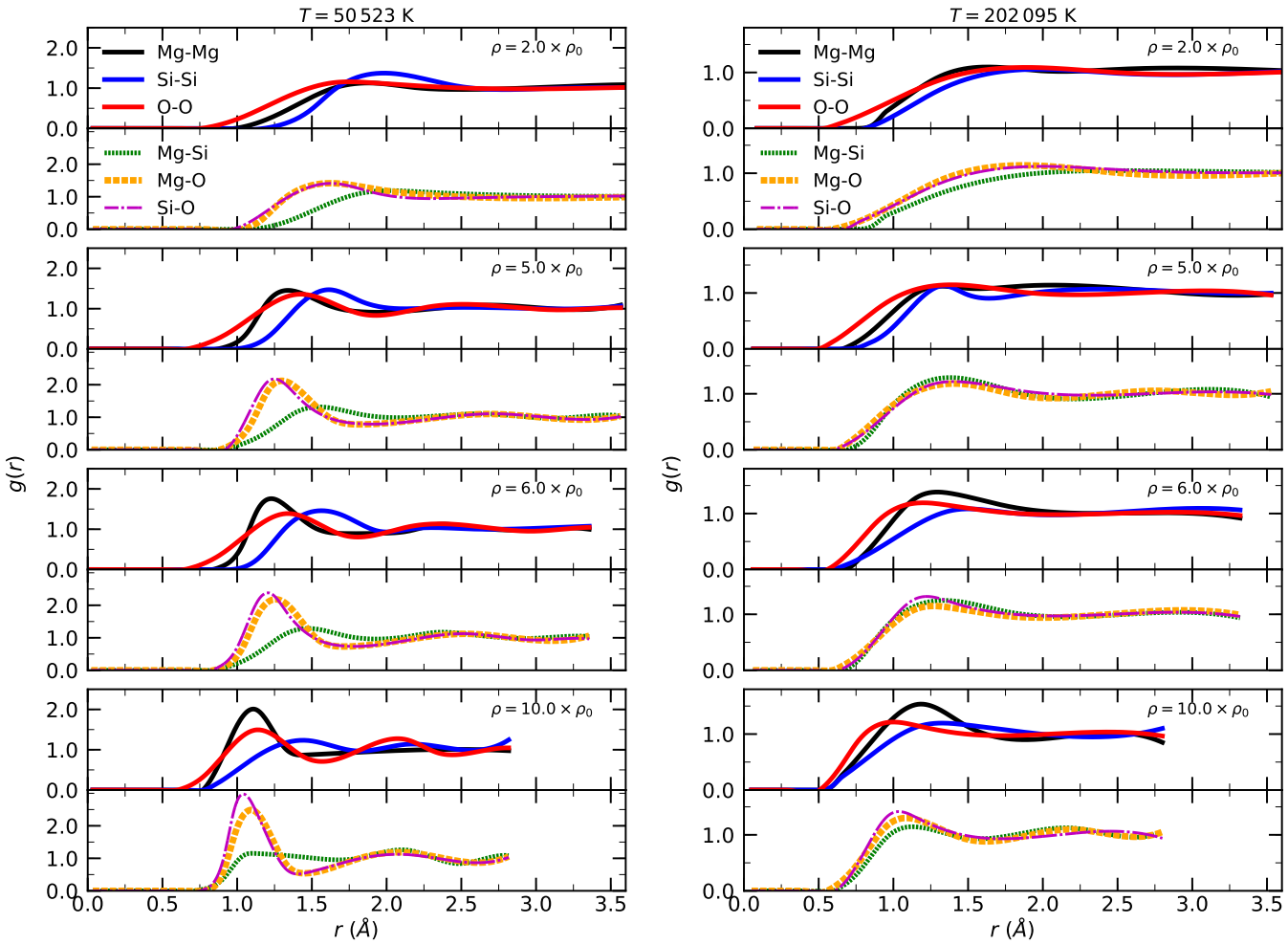

FIG. 10. Nuclear radial distribution functions computed with DFT-MD simulations of liquid $MgSiO_3$ at a fixed temperatures of 50 523 K and 202 095 K. Functions are calculated in 65-atom cells and compared for densities of (from top to bottom) 6.41 (2-fold, top), 16.04 (5-fold), 19.25 (6-fold), and 32.08 g cm^{-3} (10-fold).

Here, we solve this equation using our computed EOS table that we provide as Supplemental Material [96]. We obtain a continuous Hugoniot curve by interpolating $E(\rho, T)$ and $P(\rho, T)$ with 2D spline functions of ρ and T. We have compared several different interpolation algorithms and find the differences are negligible because our EOS table is reasonably dense. For the principal Hugoniot curve of solid enstatite, we used $P_0 = 0$, the ambient density $\rho_0 = 3.207911$ g cm^{-3} ($V_0 = 51.965073$ Å^3/f.u.), and initial internal energy E_0 = -35.914 eV/f.u. + ΔE [85], where ΔE is the shift applied to DFT-MD energies defined in section III. The resulting Hugoniot curve has been added to Figs. 1, 2, 11, and 12.

The principal Hugoniot curve in Fig. 11 exhibits a wide pressure interval where the compression ratio exceeds 4.0, the value for an ideal gas. Such high compression values are the result of excitations of internal degrees of freedom [55, 56], which increase the internal energy term in Eq. (7). Consequently, the second term in this equation becomes more negative, which reduces the volume V and thus increases the compression ratio. At a pressure of 15956 GPa and a temperature of 512 000 K, the shock compression ratio starts to exceed 4, which are conditions where the L shell electrons are ionized. The bulk of the high compression region is dominated by the ionization of the K shell (1s) electrons of the three nuclei. We see one broad region of increased compression instead of three separate peaks, one for each nucleus. We conclude that the ionization peaks are merged.

The highest compression ratio of 4.70 is reached for 5.14×10^7 K and 299 000 GPa, which coincides in pressure with the upper compression maximum of the shock Hugoniot curve of pure silicon, which has also been attributed to K shell ionization [45]. Based on this comparison and the K shell ionization analysis of $MgSiO_3$ in Fig. 8 we conclude that the upper part of the high compression region in Fig. 11 is dominated by the ionization of the K shell electrons of the Si and also the Mg nuclei, because their $N(r)$ curves in Fig. 8 are fairly similar. The lower end of the broad compression peak in Fig. 11, around 6×10^4 GPa and 1.4×10^6 K, marks the beginning of the K shell ionization of the oxygen ions as Fig. 8 confirms. However, in shock compressed pure oxygen, the K shell ionization peak occurs for lower P and T. We attribute this difference to interaction effects in hot, dense $MgSiO_3$ that can shift the compression peaks along the Hugoniot curve to higher temperatures and pressures and reduce the peak compression [55, 56]. It should also be noted that the highest compression ratio of 4.70 is reached

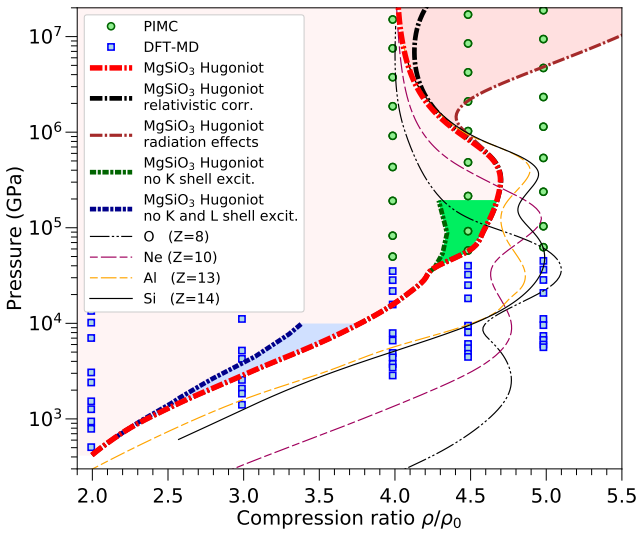

FIG. 11. Comparison of the principal shock Hugoniot curves of $MgSiO_3$ with those of carbon [44], oxygen [92], neon [83], aluminum [18], and silicon [19, 45]. **The two dash-dotted curves and shaded regions show Hugoniot curves without any electronic excitations and just without K shell ionization. Electronic excitations increase the shock compression. Without them, a maximum compression ratio of 4.7 could not be attained.**

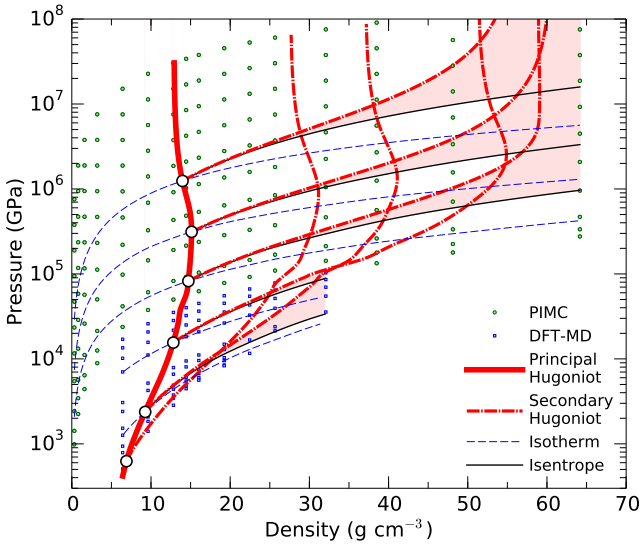

FIG. 12. Comparison of principal and secondary shock Hugoniot curves with isotherms and isentropes in pressure-density space.

when the K shell electrons of the Si and Mg nuclei are ionized, not for the lower temperature at which the K shell electrons of oxygen are ionized, even though three out of five nuclei are of that type and one could have predicted that their ionization leads to the largest compression.

We performed additional DFT-MD calculations without any electronic excitations in order to determine their effect on the shock Hugoniot curve. In Ref. [55], it was shown that electronic excitations increase to shock compression ratio of helium to 5.24 while the shock Hugoniot curve without electronic excitations never exceed 4-fold compression. In Fig. 11, we show a very similar behavior for shock compressed $MgSiO_3$. Electronic excitations start to matter at approximately 30,000 K, 2.3-fold compression, and 850 GPa. With increasing temperature, electronic excitations become more importance and the gap between the Hugoniot curves with and without excitations widens. At 10^6 K, a shock Hugoniot curve without excitations would yield a pressure of 7700 GPa, $u_p = 40.9$ km/s, $u_s = 58.7$ km/s and compression ratio of only 3.3 while with excitations, the compression ratio is 4.3 and thus the pressure reaches a much higher value of 38 000 GPa while the particle and shock velocities attain much higher values of $u_p = 95$ km/s, $u_s = 124$ km/s. These differences are a bit smaller if one compares the predictions for given particle velocity of $u_p = 40.9$ km/s, rather than for constant temperature. With electronic excitations, an increased compression ratio of 3.6 is predicted while one obtains slightly reduced values of pressure (7420 GPa) and the shock speed ($u_s = 56.6$ km/s). However, the temperature is much lower (280 000 K) than is predicted without excitation (10^6 K). This underlines that electronic excitation significantly affect the final state in shock compression experiments of dense silicates.

In Fig. 11, we also show a shock Hugoniot curve that includes L shell but no K shell ionization. This curve was derived from VASP DFT-MD simulations that relied on pseudopotentials with a frozen K shell electrons. At 4.26-fold compression, 37700 GPa, and 1.01 $\times 10^6$ K, this curve starts to deviate from our original Hugoniot curve that included the K shell ionization. It is the ionization of this shell that introduces a shoulder into the Hugoniot curve and increases the compression to a maximum value of 4.7.

Very approximately, we added relativistic and radiation effects to the Hugoniot curves in Fig. 11. Under the assumption of complete ionization, the relativistic corrections were derived for an ideal gas of electrons. This increases the shock compression ratio for $P > 4 \times 10^6$ GPa and $T > 7 \times 10^7$ K. Considering an ideal black body scenario, we derived the photon contribution to the EOS using $P_{\text{radiation}} = (4\sigma/3c)T^4$ and $E_{\text{radiation}} = 3P_{\text{radiation}}V$, where σ is the Stefan-Boltzman constant and c is the speed of light in vacuum. We find that radiation effects are important only for temperatures above 3×10^7 K, which are well above the temperature necessary to completely ionize the 1s orbitals of all atomic species.

In Fig. 2, we can observe how our calculated Hugoniot overlaps with the experimental data from Fratanduono et al. [86] who performed laser-driven shock experiments on enstatite to obtain a continuous measurement of the principal Hugoniot curve. In these experiments, enstatite was shocked up to 600 GPa reaching temperatures as high as 2×10^4 K. Using a Grüneisen parameter model coupled to an EOS, Fratanduono et al. derive isentropic profiles for liquid $MgSiO_3$ close to the melting curve. Their findings show that the melting curve and the isentropic temperature profiles, shown in Fig. 2, are shallower than previous DFT-MD predictions [97] and nearly parallel to each other, which can have substantial implications for the interior of rocky exoplanets, such as the possible crystallization of a deep silicate mantle over a wide range of temperatures.

To provide a guide for future ramp compression experiments, we also plot different isentropes, derived from the relationship $\frac{dT}{dV}\big|_S = -T\,\frac{dP}{dT}\big|_V / \frac{dE}{dT}\big|_V$ and added them to Figs. 1, 2, and 12. We find that the slope of the isentropes does not strongly depend on temper-

ature, even though we compare conditions with differing degrees of ionization. Our results imply that the temperature rise with pressure along the isentropes approximately follows a power law, $T \propto P^{\alpha}$, with an exponent $\alpha = 0.309$ below 10^6 K, increasing only up to $\alpha = 0.399$ for temperatures above 10^7 K. This provides simple rule for obtaining isentropic profiles in $MgSiO_3$ with wide-range validity, without the need of relying in approximate models.

In Fig. 12, we show a number of double-shock Hugoniot curves. Various points on the principal Hugoniot curve were chosen as initial conditions for a second shock that compresses the material again, reaching densities that are much higher than those that can probed with single shocks. If one starts from the high compression point on the principal Hugoniot curve, one can reach densities of 60 g cm^{-3}. However, the compression ratio is typically not as high because the strength of the interaction effects increases and this lowers the compression ratio. For the secondary shock Hugoniot curves that we show in Fig. 12, the maximum compression ratio varied between 4.44 and 4.01 while the maximum compression ratio of the principlal Hugoniot curve was 4.70.

Fig. 12 also compares our secondary Hugoniot curves with our isentropes and isotherms. For weak second shocks, the secondary Hugoniot curves and isentropes almost coincide, which implies that the second shock produces very little nonreversible heat. As the strength of the second shock increases, more and more nonreversible heat is generated.

To provide a direct comparison with experiments, we also derived the particle velocity, u_p, and shock velocity, u_s, along the principal Hugoniot curve. The left panel of Fig. 13 shows the particle velocity as a function of compression ratio, which allows on to related the prediction to Fig. 11. It is often found that u_p and u_s follow an approximately linear relationship over a wide range of conditions [86, 98]. However, one does not expect a linear relationship to hold perfectly when electronic excitations introduce distinct increases in compression at well-defined temperature/pressure intervals. Therefore we first fit a linear u_p-u_s relation for our computed Hugoniot curve and then plot the deviation from it in the right panel of Fig. 13. The comparison of both panels allows us to correlate deviations from linear u_p-u_s relation with changes in compression. For example the onset of the K shell ionization that introduces a bump into the Hugoniot curve at 4.3-fold compression also leads to a bump in u_s for u_p = 90 km/s. Similarly, when the K shell ionization of the oxygen atom increase the compression ratio to 4.6, we see a reduction in u_s for u_p = 140 km/s. Finally, the ionization of the Mg and Si K shell electrons that leads to the compression maximum of 4.7 $\times\rho_0$ also leads to a reduction in u_s for u_p = 270 km/s. For even higher particle velocities, the system approaches the states of a completely ionized plasma where the shock compression ratio is gradually reduced to 4 and our linear u_p-u_s relation does no longer hold.

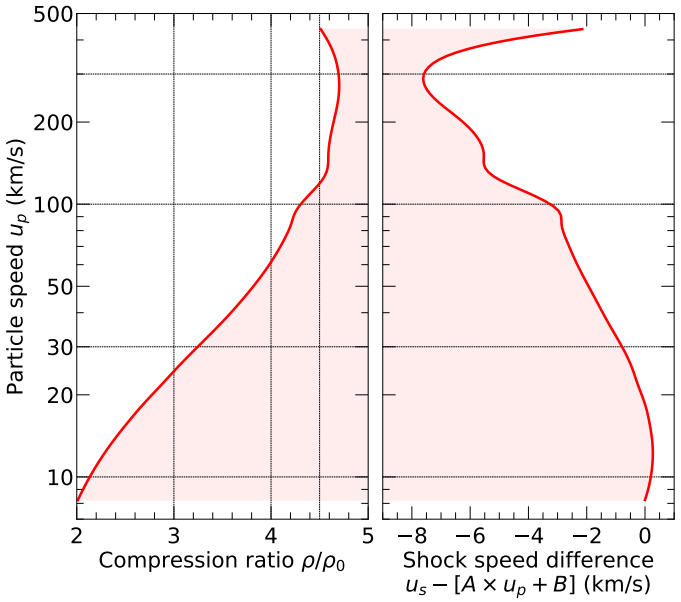

FIG. 13. On the left, particle velocity u_p is shown a function of compression ratio. On the right, we show the deviations from a linear u_p-u_s fit. The coefficients were $A = 1.2764$ and $B = 8.2315$ km/s.

VII. SPECIFIC HEAT

The specific heat, $C_v = \frac{\partial E}{\partial T}\big|_V$ is shown in Fig. 14 as a function of temperature for various densities. For temperatures below 10^5 K, our calculations show that the value of C_v approaches 21 k_B/f.u. (4.2 k_B/atom) at 2-fold compression (6.42 g cm^{-3}), which is in agreement with previous DFT calculations [90] and recent experimental measurements [86] along the Hugoniot at similar conditions. At very high temperatures, where the all atomic species are completely ionized, we recover the expected nonrelativistic limit of $\frac{3}{2}Nk_b$, where $N = 55$ is the total number of free particles of the $MgSiO_3$ system (5 nuclei and 50 electrons).

As electrons become free with increasing temperature, the specific heat increases, reaching a local maximum at around $T \approx 2 \times 10^6$ K for the density range of 0.1–2ρ_0, which reflects the ionization of K shell electrons of the oxygen atoms. This peak dissapears almost completely at $4\rho_0$ because this compression prevents the oxygen K shell electrons from becoming ionized, as we discussed in the previous section. A second maximum appears around $T \approx 7 \times 10^6$ K, which can be associated with the almost simultaneous ionization of Mg and Si K shell electrons, as we showed in Fig. 8.

In the bottom panel of Fig. 14, we observe that the Grüneisen parameter, γ, decreases with temperature up to approximately 2×10^6 K for all densities considered, due to the increasing value of C_v (see Eq. (4)). Above 2×10^6 K, where ionization of the K shells takes place, γ increases with temperature due to the decrease in C_v and tends to the ideal gas limit of $\gamma_0 = 2/3$, as we have shown in Fig. 7.

A discontinuity in the principal Hugoniot of liquid $MgSiO_3$ has been observed around 15000 K and 500 GPa [38], which was interpreted as a liquid–liquid phase transition that could lead to an unusually large increase of the specific heat. According to this study, C_v could be as large as 90 k_B/f.u. (18 k_B/atom) at these conditions, a value that is expected only at temperatures beyond 10^6 K, according to our calculations. However, this transition has not been confirmed in previous DFT-MD simulations [85], and recent experiments [86, 99] show no anomalies in the principal Hugoniot that could support this hypothesis. Therefore, we should expect C_V to be at most 30 k_B/f.u. (6 k_B/atom) below 100 000 K.

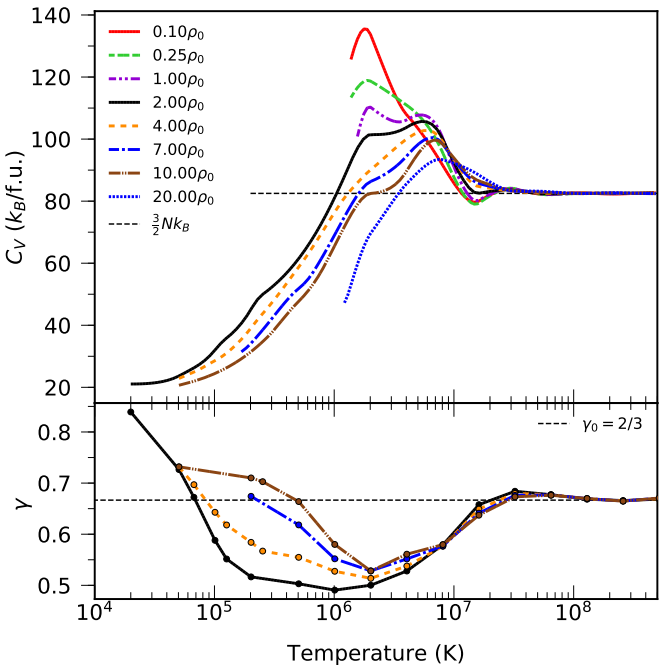

FIG. 14. Heat capacity and Grüneisen parameter temperature dependence, derived from DFT-MD and PIMC calculations at various densities. The horizontal dashed line in the upper panel represents the high temperature limit of $C_V = \frac{3}{2}Nk_B$ where $N = 55$ is the total number of free particles per $MgSiO_3$ formula unit, with 5 ions and 50 electrons. Values above this line mark the temperature region of ionization where the intenal energy increases significantly. In the lower panel, the Grüneisen parameter of the ideal gas, $\gamma_0 = 2/3$, also represents the high temperature limit.

VIII. CONCLUSIONS

We have constructed a consistent EOS of $MgSiO_3$ over a wide temperature-density range using DFT-MD and PIMC that bridges the WDM and plasma regimes. **Our results provide the first detailed characterization of K shell ionization in a triatomic material. We quantify the degree of ionization and the contribution from each atomic species to the thermodynamic properties, which, at the present time, cannot be inferred from the laboratory experiments. We predict that the maximum compression ratio for enstatite is 4.7, which is attained for** 5.13×10^6 **K and** 3.01×10^5 **GPa in the WDM regime. By performing additional calculations without any electronic excitations or only without K shell excitations, we are able to determine the conditions where these excitations start to increase the shock compression. We show that without electronic excitations the shock compression ratio of $MgSiO_3$ would not exceed 4.0. Excitations of L shell electrons start increase the shock compression from 30,000 K, 847 GPa,** $\rho/\rho_0 = 2.28$, $u_p = 12.2$ **km/s and** $u_s = 21.7$ **km/s onwards, which is within the reach of current laboratory experiments. It is also interesting to note that we do not see a separate L shell ionization peak. We conclude that this shell is ionized gradually, as it occurs in dense carbon and boron materials [8, 64, 65, 100]. Excitations of K shell electrons set in at 1.01** $\times 10^6$ **K, 37700 GPa,** $\rho/\rho_0 = 4.26$, $u_p = 94.8$ **km/s and** $u_s = 124$ **km/s.**

We find good agreement between results from PIMC and DFT-MD simulations, which provides evidence that the combination of these two different formulations of quantum mechanics can be used to accurately describe WDM. The precision of first-principles computer simulations will guide the design of inertial confinement fusion (ICF) experiments under conditions where the K and L shell electrons are gradually ionized, which is challenging to predict accurately with analytical EOS models.

We showed that PIMC and DFT-MD simulations produce consistent EOS data in the 1–2 $\times 10^6$ K temperature range, validating the use of the fixed-node approximation in PIMC and zero-temperature XC functionals in DFT-MD for warm dense $MgSiO_3$. We obtain a shock Hugoniot curve that is consistent with experiments and includes the K shell ionization regime of the three atomic species. Their ionization leads a one broad peak of high compression ratios between 4.5 and 4.7. The maximum compression is reached for higher temperatures, where the Mg and Si atoms are ionized, even though there are more oxygen atoms present and their 1s ionization occurs at slightly lower temperatures.

Subsequently, we analyzed how close a secondary shock Hugoniont curves can stay to an isentrope, providing a guide for future ramp compression experiments. We also showed that the Grüneisen parameter increases upon compression for most of the temperatures analyzed in this study, and converges to the ideal gas limit when temperature reaches $\sim 2 \times 10^7$, consistent with a full K shell ionization of all atomic species.

Finally, we then studied heat capacity and pair-correlation functions to reveal the evolution of the fluid structure and ionization behavior. Overall, we demonstrate that PIMC is an predictive tool to determine the EOS in the WDM regime. We demonstrated that He-core PBE functional can accurately describe $MgSiO_3$ up to temperatures of $\sim 10^6$ K. For higher temperature, the ionization of K shell electrons significantly affect the thermodynamic properties and the shock Hugoniot curve of $MgSiO_3$ and the frozen-core approximation in the pseudopotential no longer valid.

ACKNOWLEDGMENTS

This work was in part supported by the National Science Foundation-Department of Energy (DOE) partnership for plasma science and engineering (grant DE-SC0016248), by the DOE-National Nuclear Security Administration (grant DE-NA0003842), and the University of California Laboratory Fees Research Program (grant LFR-17-449059). We thank the authors of Ref. [86] for providing the full data set from their experiments. F.G.-C. acknowledges support from the CONICYT Postdoctoral fellowship (grant 74160058). Computational support was provided by the Blue Waters sustained-petascale computing project (NSF ACI 1640776) and the National Energy Research Scientific Computing Center.

REFERENCES

[1] S. Mazevet, A. Licari, G. Chabrier, and A. Y. Potekhin, Astronomy & Astrophysics **621**, A128 (2019).
[2] S. Seager, M. Kuchner, C. A. Hier-Majumder, and B. Militzer, The Astrophysical Journal **669**, 1279 (2007).
[3] A. Benuzzi-Mounaix, S. Mazevet, A. Ravasio, T. Vinci, A. Denoeud, M. Koenig, N. Amadou, E. Brambrink, F. Festa, A. Levy, *et al.*, Physica Scripta **2014**, 014060 (2014).
[4] M. Cotelo, P. Velarde, A. de La Varga, and C. García-Fernández, Astrophysics and Space Science **336**, 53 (2011).
[5] G. Chabrier, F. Douchin, and A. Potekhin, Journal of Physics: Condensed Matter **14**, 9133 (2002).
[6] L. Kirsch, S. Ali, D. Fratanduono, R. Kraus, D. Braun, A. Fernandez-Pañella, R. Smith, J. McNaney, and J. Eggert, Journal of Applied Physics **125**, 175901 (2019).
[7] M. Millot, N. a. Dubrovinskaia, A. Černok, S. Blaha, L. Dubrovinsky, D. Braun, P. Celliers, G. Collins, J. Eggert, and R. Jeanloz, Science **347**, 418 (2015).
[8] S. Zhang, B. Militzer, M. C. Gregor, K. Caspersen, L. H. Yang, J. Gaffney, T. Ogitsu, D. Swift, A. Lazicki, D. Erskine, R. A. London, P. M. Celliers, J. Nilsen, P. A. Sterne, and H. D. Whitley, Phys. Rev. E **98**, 023205 (2018).
[9] R. Betti and O. Hurricane, Nature Physics **12**, 435 (2016).
[10] P. Seidl, A. Anders, F. Bieniosek, J. Barnard, J. Calanog, A. Chen, R. Cohen, J. Coleman, M. Dorf, E. Gilson, *et al.*, Nuclear Instruments and Methods in Physics Research Section A: Accelerators, Spectrometers, Detectors and Associated Equipment **606**, 75 (2009).
[11] K. Miyanishi, Y. Tange, N. Ozaki, T. Kimura, T. Sano, Y. Sakawa, T. Tsuchiya, and R. Kodama, Phys. Rev. E **92**, 023103 (2015).
[12] R. Feynman and A. Hibbs, *Quantum Mechanics and Path integrals*, International series in pure and applied physics (McGraw-Hill, New York, 1965).
[13] D. M. Ceperley, Journal of Statistical Physics **63**, 1237 (1991).
[14] C. Pierleoni, D. M. Ceperley, B. Bernu, and W. R. Magro, Phys. Rev. Lett. **73**, 2145 (1994).
[15] C. Rickwardt, P. Nielaba, M. H. Müser, and K. Binder, Phys. Rev. B **63**, 045204 (2001).
[16] B. Militzer and D. M. Ceperley, Phys. Rev. Lett. **85**, 1890 (2000).
[17] K. P. Driver and B. Militzer, Phys. Rev. E **95**, 043205 (2017).
[18] K. P. Driver, F. Soubiran, and B. Militzer, Phys. Rev. E **97**, 063207 (2018).
[19] K. P. Driver, F. Soubiran, S. Zhang, and B. Militzer, High Energy Density Physics **23**, 81 (2017).
[20] H. F. Wilson, M. L. Wong, and B. Militzer, Phys. Rev. Lett. **110**, 151102 (2013).
[21] M. Millot, S. Hamel, J. R. Rygg, P. M. Celliers, G. W. Collins, F. Coppari, D. E. Fratanduono, R. Jeanloz, D. C. Swift, and J. H. Eggert, Nature Physics **14**, 297 (2018).
[22] T. S. Duffy and R. F. Smith, Frontiers in Earth Science **7**, 1 (2019).
[23] T. Duffy, N. Madhusudhan, and K. Lee, in *Treatise on Geophysics*, Vol. 2 (Elsevier, 2015) pp. 149–178.
[24] S. N. Luo, J. A. Akins, T. J. Ahrens, and P. D. Asimow, Journal of Geophysical Research: Solid Earth **109**, 1 (2004).
[25] R. Kraus, S. Stewart, D. Swift, C. Bolme, R. Smith, S. Hamel, B. Hammel, D. Spaulding, D. Hicks, J. Eggert, *et al.*, Journal of Geophysical Research: Planets **117** (2012).
[26] F. Molster, T. Lim, R. Sylvester, L. Waters, M. Barlow, D. Beintema, M. Cohen, P. Cox, and B. Schmitt, Astronomy & Astrophysics **372**, 165 (2001).
[27] D. Valencia, M. Ikoma, T. Guillot, and N. Nettelmann, Astronomy & Astrophysics **516**, A20 (2010).
[28] R. M. Bolis, G. Morard, T. Vinci, A. Ravasio, E. Bambrink, M. Guarguaglini, M. Koenig, R. Musella, F. Remus, J. Bouchet, N. Ozaki, K. Miyanishi, T. Sekine, Y. Sakawa, T. Sano, R. Kodama, F. Guyot, and A. Benuzzi-Mounaix, Geophysical Research Letters **43**, 9475 (2016).
[29] D. Valencia, R. J. O'Connell, and D. D. Sasselov, Astrophysics and Space Science **322**, 135 (2009).
[30] R. F. Smith, D. E. Fratanduono, D. G. Braun, T. S. Duffy, J. K. Wicks, P. M. Celliers, S. J. Ali, A. Fernandez-Pañella, R. G. Kraus, D. C. Swift, G. W. Collins, and J. H. Eggert, Nature Astronomy (2018).
[31] D. G. Hicks, T. R. Boehly, J. H. Eggert, J. E. Miller, P. M. Celliers, and G. W. Collins, Phys. Rev. Lett. **97**, 025502 (2006).
[32] D. C. Swift, R. G. Kraus, E. N. Loomis, D. G. Hicks, J. M. McNaney, and R. P. Johnson, Phys. Rev. E **78**, 066115 (2008).
[33] S. D. Rothman, J. P. Davis, J. Maw, C. M. Robinson, K. Parker, and J. Palmer, Journal of Physics D: Applied Physics **38**, 733 (2005).
[34] D. K. Bradley, J. H. Eggert, R. F. Smith, S. T. Prisbrey, D. G. Hicks, D. G. Braun, J. Biener, A. V. Hamza, R. E. Rudd, and G. W. Collins, Phys. Rev. Lett. **102**, 075503 (2009).
[35] R. F. Smith, J. H. Eggert, R. Jeanloz, T. S. Duffy, D. G. Braun, J. R. Patterson, R. E. Rudd, J. Biener, a. E. Lazicki, a. V. Hamza, J. Wang, T. Braun, L. X. Benedict, P. M. Celliers, and G. W. Collins, Nature **511**, 330 (2014).
[36] F. W. Wagner, N. Tosi, F. Sohl, H. Rauer, and T. Spohn, Astronomy & Astrophysics **541**, A103 (2012).
[37] W. B. Hubbard, *Planetary Interiors* (University of Arizona Press, Tucson, AZ, 1984).
[38] D. K. Spaulding, R. S. McWilliams, R. Jeanloz, J. H. Eggert, P. M. Celliers, D. G. Hicks, G. W. Collins, and R. F. Smith, Phys. Rev. Lett. **108**, 065701 (2012).
[39] S. Root, J. P. Townsend, E. Davies, R. W. Lemke, D. E. Bliss, D. E. Fratanduono, R. G. Kraus, M. Millot, D. K. Spaulding, L. Shulenburger, S. T. Stewart, and S. B. Jacobsen, Geophysical Research Letters **45**, 3865 (2018).
[40] J. L. Mosenfelder, P. D. Asimow, D. J. Frost, D. C. Rubie, and T. J. Ahrens, Journal of Geophysical Research: Solid Earth **114**, 1 (2009).
[41] T. Tsuchiya, J. Tsuchiya, K. Umemoto, and R. M. Wentzcovitch, Earth and Planetary Science Letters **224**, 241 (2004).
[42] K. Umemoto, R. M. Wentzcovitch, S. Wu, M. Ji, C.-z. Wang, and K.-m. Ho, Earth and Planetary Science Letters **478**, 40 (2017).
[43] F. Soubiran and B. Militzer, Nature Communications **9**, 3883 (2018).
[44] K. P. Driver and B. Militzer, Phys. Rev. Lett. **108**, 115502 (2012).
[45] B. Militzer and K. P. Driver, Phys. Rev. Lett. **115**, 176403 (2015).
[46] F. Soubiran, F. González-Cataldo, K. P. Driver, S. Zhang, and B. Militzer, The Journal of Chemical Physics **151**, 214104 (2019).
[47] E. L. Pollock and D. M. Ceperley, Phys. Rev. B **30**, 2555 (1984).
[48] D. M. Ceperley, Rev. Mod. Phys. **67**, 279 (1995).
[49] D. M. Ceperley, Phys. Rev. Lett. **69**, 331 (1992).
[50] D. Ceperley (Editrice Compositori, Bologna, Italy, 1996) p. 443.
[51] W. R. Magro, D. M. Ceperley, C. Pierleoni, and B. Bernu, Phys. Rev. Lett. **76**, 1240 (1996).
[52] B. Militzer, W. Magro, and D. Ceperley, Contributions to Plasma Physics **39**, 151 (1999).
[53] B. Militzer and D. M. Ceperley, Phys. Rev. E **63**, 066404 (2001).
[54] B. Militzer, D. M. Ceperley, J. D. Kress, J. D. Johnson, L. A. Collins, and S. Mazevet, Phys. Rev. Lett. **87**, 275502 (2001).
[55] B. Militzer, Phys. Rev. Lett. **97**, 175501 (2006).
[56] B. Militzer, Phys. Rev. B **79**, 155105 (2009).
[57] B. Militzer, Journal of Physics A: Mathematical and Theoretical **42**, 214001 (2009).
[58] B. Militzer, Journal of Low Temperature Physics **139**, 739 (2005).
[59] M. D. Jones and D. M. Ceperley, Phys. Rev. Lett. **76**, 4572 (1996).
[60] E. L. Pollock and B. Militzer, Phys. Rev. Lett. **92**, 021101 (2004).
[61] B. Militzer and E. L. Pollock, Phys. Rev. B **71**, 134303 (2005).

[62] L. X. Benedict, K. P. Driver, S. Hamel, B. Militzer, T. Qi, A. A. Correa, A. Saul, and E. Schwegler, Phys. Rev. B **89**, 224109 (2014).
[63] K. P. Driver and B. Militzer, Phys. Rev. B **93**, 064101 (2016).
[64] S. Zhang, K. P. Driver, F. Soubiran, and B. Militzer, Phys. Rev. E **96**, 013204 (2017).
[65] S. Zhang, B. Militzer, L. X. Benedict, F. Soubiran, P. A. Sterne, and K. P. Driver, J. Chem. Phys. **148**, 102318 (2018).
[66] S. X. Hu, B. Militzer, L. A. Collins, K. P. Driver, and J. D. Kress, Phys. Rev. B **94**, 094109 (2016).
[67] S. Zhang, K. P. Driver, F. Soubiran, and B. Militzer, J. Chem. Phys. **146**, 074505 (2017).
[68] V. Natoli and D. M. Ceperley, Journal of Computational Physics **117**, 171 (1995).
[69] B. Militzer, Comp. Phys. Comm. **204**, 88 (2016).
[70] B. Militzer, E. Pollock, and D. Ceperley, High Energy Density Physics **30**, 13 (2019).
[71] P. Hohenberg and W. Kohn, Phys. Rev. **136**, B864 (1964).
[72] W. Kohn and L. J. Sham, Phys. Rev. **140**, A1133 (1965).
[73] N. D. Mermin, Phys. Rev. **137**, A1441 (1965).
[74] S. Root, R. J. Magyar, J. H. Carpenter, D. L. Hanson, and T. R. Mattsson, Phys. Rev. Lett. **105**, 085501 (2010).
[75] X. Wang, F. Tian, L. Wang, T. Cui, B. Liu, and G. Zou, J. Chem. Phys. **132**, 024502 (2010).
[76] T. R. Mattsson, S. Root, A. E. Mattsson, L. Shulenburger, R. J. Magyar, and D. G. Flicker, Phys. Rev. B **90**, 184105 (2014).
[77] V. V. Karasiev, L. Calderín, and S. B. Trickey, Phys. Rev. E **93**, 063207 (2016).
[78] B. Militzer, *Path Integral Monte Carlo Simulations of Hot Dense Hydrogen*, Ph.D. thesis, University of Illinois at Urbana-Champaign (2000).
[79] G. Kresse and J. Furthmüller, Phys. Rev. B **54**, 11169 (1996).
[80] P. E. Blöchl, Phys. Rev. B **50**, 17953 (1994).
[81] G. Kresse and D. Joubert, Phys. Rev. B **59**, 1758 (1999).
[82] J. P. Perdew, K. Burke, and M. Ernzerhof, Phys. Rev. Lett. **77**, 3865 (1996).
[83] K. P. Driver and B. Militzer, Phys. Rev. B **91**, 045103 (2015).
[84] For OPIUM pseudopotential generation programs, see http://opium.sourceforge.net.
[85] B. Militzer, High Energy Density Physics **9**, 152 (2013).
[86] D. E. Fratanduono, M. Millot, R. G. Kraus, D. K. Spaulding, G. W. Collins, P. M. Celliers, and J. H. Eggert, Phys. Rev. B **97**, 214105 (2018).
[87] A. B. Belonoshko, N. V. Skorodumova, A. Rosengren, R. Ahuja, B. Johansson, L. Burakovsky, and D. L. Preston, Phys. Rev. Lett. **94**, 195701 (2005).
[88] P. Debye and E. Hückel, Phys. Z **24**, 185 (1923).
[89] R. S. McWilliams, D. K. Spaulding, J. H. Eggert, P. M. Celliers, D. G. Hicks, R. F. Smith, G. W. Collins, and R. Jeanloz, Science **338**, 1330 (2012).
[90] N. de Koker and L. Stixrude, Geophysical Journal International **178**, 162 (2009).
[91] W. Ebeling, W. Kraeft, and D. Kremp, Ergebnisse der Plasmaphysik und der Gaselektronik, Band 5 (Akademie-Verlag, Berlin, 1976).
[92] K. P. Driver, F. Soubiran, S. Zhang, and B. Militzer, J. Chem. Phys. **143**, 164507 (2015).
[93] General Atomic and Molecular Electronic Structure System (GAMESS). Visit http://www.msg.ameslab.gov/gamess/ for more information.
[94] L. Stixrude and B. Karki, Science **310**, 297 (2005).
[95] Y. B. Zeldovich and Y. P. Raizer, *Elements of Gasdynamics and the Classical Theory of Shock Waves* (Academic Press, New York, 1968).
[96] See Supplemental Material at [URL will be inserted by publisher] for internal energy and pressure predictions, as computed by both DFT-MD and PIMC.
[97] L. Stixrude, Philosophical Transactions of the Royal Society A: Mathematical, Physical and Engineering Sciences **372**, 20130076 (2014).
[98] W. Nellis, N. Holmes, A. Mitchell, R. Trainor, G. Governo, M. Ross, and D. Young, Physical Review Letters **53**, 1248 (1984).
[99] D. K. Spaulding, R. S. McWilliams, R. Jeanloz, J. H. Eggert, P. M. Celliers, D. G. Hicks, G. W. Collins, and R. F. Smith, Phys. Rev. Lett. **119**, 139903(E) (2017).
[100] S. Zhang, A. Lazicki, B. Militzer, L. H. Yang, K. Caspersen, J. A. Gaffney, M. W. Däne, J. E. Pask, W. R. Johnson, A. Sharma, P. Suryanarayana, D. D. Johnson, A. V. Smirnov, P. A. Sterne, D. Erskine, R. A. London, F. Coppari, D. Swift, J. Nilsen, A. J. Nelson, and H. D. Whitley, Phys. Rev. B **99**, 165103 (2019).